J Mater Sci (2009) 44:2780–2791
DOI 10.1007/s10853-009-3366-2

Changes in material properties and surface fractality of multi-walled carbon nanotubes modified by heat and acid treatments

Yu-Chun Chiang · Chen-Yueh Lee

Received: 2 December 2008 / Accepted: 23 February 2009 / Published online: 19 March 2009

Abstract Heat treatment and acid oxidation of multi-walled carbon nanotubes (MWNTs) were conducted in this study. Fractal analysis was carried out to study the surface properties of the MWNTs after modifications. The results of the present work show that there was a contraction in the hysteresis loop at P/P_o around 0.80, which differentiated the capillary condensation in the internal pores from that in the aggregated pores forming by the entangled MWNTs. The maximum of the pore size distribution (PSD) curves in the mesopore range did not shift after modification because it described the major inner diameters of the MWNTs. A smooth and ordered surface could be formed after heat treatment, but a much rougher and less homogeneous surface was produced on acid-treated MWNTs. Moreover, an excellent linear increase in the surface fractal dimension (d_s) values was observed as the micropore surface area (S_{mi}) increased, which implies that the generation of micropores would contribute to the surface roughness.

Introduction

The discovery of carbon nanotubes (CNTs) has stimulated intensive research on the synthesis, modification, and properties of these novel carbon materials [1]. Due to their light weight, small size, relatively large surface area, and hollow geometry, CNTs have been considered as alternative materials for gas adsorption [2–6], gas sensing [7], separation processes [8], or as catalyst supports [9]. Since these applications are highly dependent on the surface features of CNTs, there is considerable interest in understanding their surface properties and porosity. Several studies have focused on the outer surface and the ends of the nanotubes [10]. Even so, the smooth and inert surface of the CNTs has restricted their applications. Therefore, the surface modification of the CNTs is necessary to improve their performance, and heat treatment or acid treatment has become one of the widely used techniques [11, 12]. For instance, the acid-treated multi-walled carbon nanotubes (MWNTs) were able to be well dispersed in a polymer matrix [13], and the C–COOH groups on MWNTs were used as a template for the formation of polyaniline/MWNTs composites [7].

Many methods have been developed to characterize porous materials, and of these methods, the nitrogen adsorption technique can provide the most of information. Recently, much attention has been paid to the application of fractal analysis to surface science [14, 15]. Fractal geometry is a key parameter affecting the interactions between adsorbed molecules and a surface [16], which can be determined by N_2 adsorption [14]. In general, the value of the surface fractal dimension (d_s) varies from two for a perfectly smooth surface to three for a very rough surface [17], so the d_s can be considered as a measure of surface roughness. It has been reported that the porous coal had a d_s of 2.4 [18], and that in the metamorphosed rocks was about 2.8 [19].

According to the modified Frenkel–Halsey–Hill (FHH) theory [20], an expression for the d_s from an analysis of multilayer adsorption in the N_2 adsorption isotherm to a fractal surface is given in Eq. 1.

Y.-C. Chiang (✉) · C.-Y. Lee
Department of Mechanical Engineering and Yuan Ze Fuel Cell Center, Yuan Ze University, 135 Yuan-Tung Rd., Chung-Li, Taoyuan 320, Taiwan
e-mail: ycchiang@saturn.yzu.edu.tw

$$\ln\left(\frac{V}{V_m}\right) = C + A\ln\left[\ln\left(\frac{P_o}{P}\right)\right] \quad (1)$$

where P is the adsorption equilibrium pressure of a gas, P_o is the saturation pressure of the gas at the given temperature, V is the volume of gas adsorbate at an equilibrium pressure P, V_m is the volume of gas in a monolayer, C is the pre-exponential factor, and A is a power law exponent dependent on d_s and the mechanism of adsorption. If surface tension (or capillary condensation) effects are significant, the relationship between A and d_s can be expressed as follows:

$$A = d_s - 3 \quad (2)$$

The d_s values depend on the number of adsorbed layers, n. The use of modified FHH theory is suggested to determine the d_s only around monolayer coverage ($1 \leq n \leq 2$) [17]. Another approach to calculating the fractal dimension is the so-called thermodynamic method, as proposed by Neimark et al. [21]. The limitation of Neimark's method is that it is valid only for describing the capillary condensation mechanism because the surface forces are not considered [15]. Neimark's equation describes a simple relationship between the surface area of the adsorbed liquid film (S) and the mean radius of the curvature of this adsorbed film (r), as follows:

$$\ln S = B - (d_{cc} - 2)\ln r \quad (3)$$

where d_{cc} denotes the fractal dimension value from the capillary condensation region of the adsorption, and B is a constant. In Eq. 3, the surface area of the film is calculated from the Kiselev equation

$$S = \frac{RT}{\gamma}\int_{N(P/P_o)}^{N_{max}} \ln\left(\frac{P_o}{P}\right) dN \quad (4)$$

where N_{max} is the amount adsorbed when P/P_o approaches unity, and γ denotes the surface tension of the liquid adsorbate. Moreover, the Kelvin equation [22] is used to convert the equilibrium pressure (P) to the mean radius of the curvature (r).

Surface fractal analysis has recently been used to investigate detailed surface information of CNTs. For example, Kukovecz et al. [23] used fractal dimensions to understand the effect of ball milling on CNTs and reported that the d_s values increased with increasing roughness of the surface. Kanyó et al. [24] found that the character of the MWNT surface gradually turned from hydrophilic into hydrophobic upon heating in N_2. Thermal treatment did not affect the d_s values of MWNTs, but their d_{cc} values decreased monotonically with increasing temperature. This implied the broad pore size distribution (PSD) curves were responsible for the low d_{cc} values. The change in the d_{cc} values of the CNTs adsorbed with poly(acrylic acid) was discussed by Hou et al. [16]. But the scale in y-axis of their Neimark's plot was much smaller than other studies, such as Lee et al. [15] or Kanyó et al. [24]. Furthermore, Hou et al. [16] thought the enhancement of the surface roughness could be supported by the increase of d_{cc}, though this explanation was not in agreement with other studies.

The surface morphology and chemistry of MWNTs are a key feature in nanotube applications. Though Yang et al. [25] reported the aggregated pores were responsible for about 80% of the total adsorption amount, a systematic investigation of the structural modification of the MWNTs after acid oxidation or heat treatment is of great importance. The present study investigates surface structure characterization of as-received and treated MWNTs. The properties of the samples were fully characterized with high-resolution transmission electron microscopy (HRTEM), X-ray diffraction (XRD) analysis, X-ray photoelectron spectroscopy (XPS) analysis and nitrogen adsorption/desorption isotherms. In order to determine the PSD curves, the Barret–Joyner–Halenda (BJH) method [22] and the Horvath–Kawazoe (HK) method [26] were utilized in mesopore and micropore ranges, respectively. Also, the d_s and d_{cc} values were derived from N_2 adsorption isotherms.

Experimental

Modifications of multi-walled carbon nanotubes

The MWNT samples were provided by Conyuan Biochemical Technology Co. of Taiwan, and were modified by means of heat treatment and wet chemical oxidation. The as-received samples (denoted by CBT) were subjected to the heat treatment to 900 °C at a heating rate of 20 °C/min in an argon or carbon dioxide atmosphere or in vacuum, soaked for 1 h, and then cooled in flowing nitrogen gas to room temperature. The obtained samples were denoted as CBT-Ar, CBT-CO_2, or CBT-Vac, respectively. Except for the treatment in vacuum, the argen or carbon dioxide was added in advance to the system for 1 h before the heat treatment started, in order to expel the air from the oven. For the wet oxidation treatment, as-received samples were impregnated with a 4 M acid solution, including sulfuric acid, nitric acid, or a mixture of sulfuric and nitric acids (1:1 by volume). Then the mixture was heated and refluxed at boiling temperature for 24 h [27]. After that, the oxidized samples were thoroughly rinsed with an excess of deionized water until the pH value of the filtrate reached ca. 7. Then the sample was dried at 103 °C in vacuum for 24 h. To make sure the samples were completely dried, the samples reacting with the solutions containing sulfuric acid were heated to 450 °C at a heating rate of 20 °C/min in a

nitrogen atmosphere and maintained for 4 h. The samples oxidized with sulfuric acid, nitric acid, or the mixture of sulfuric and nitric acids were denoted as CBT-S, CBT-N, or CBT-SN, respectively. The weight losses of treated MWNTs were 19.3–22.5% for CBT-Ar, 26.1–28.5% for CBT-CO_2, ~3% for CBT-Vac, 16.9–23.0% for CBT-S, 17.4–19.6% for CBT-N, and 13.8–14.2% for CBT-SN.

Characterization of MWNTs

The microstructure of the MWNTs was examined with a high-resolution transmission electron microscope (Philips, Tecnai G2, 200 kV). Specimens for HRTEM observation were prepared by the following procedures. A portion of the MWNT samples was ultrasonicated in acetone for 1 h, and then the diluted suspension was drop-dried on a sample grid which is a holey carbon-coated copper grid.

X-ray diffraction analysis was conducted in order to determine the effects of the treatments on the nanotubes and their crystalline organization. The sharpness and shape of peaks in the XRD patterns are determined by crystal perfection. Defects or disorder in crystals will result in diffuse scattering and a broader peak. The XRD patterns were taken with a Siemens D5000 Diffractometer, which provides the atomic spacing in crystals using diffraction of approximately monochromatic X-radiation. This instrument is useful for both powders and bulk materials. The radiation used was Cu K_α with a wavelength of 0.15418 nm. The 2-theta (2θ) ranged from 10 to 80 degrees, where θ is the diffraction angle.

X-ray photoelectron spectroscopy was employed to determine the chemical composition present on the outermost surface or at the tips of the MWNTs samples. The XPS spectra of all samples were acquired using a spectrophotometer (VG Scientific ESCALAB 210) with a micofocus monochromator Al K_α X-ray source (hv = 1486.68 eV). The survey scan spectra were collected at the binding energy (B.E.) of 0–1,000 eV with a step size of 1 eV, in order to identify the elements present on the surface and in the sub-superficial zone of the MWNTs. The atomic ratios were calculated from the photoelectron peak area, using sensitivity factors according to the transmission characteristics of the Physical Electronics SCA [28].

The XPS survey spectra showed prominent peaks due to carbon and oxygen only, and so the high-resolution XPS spectra of C 1s were acquired over 278–296 eV with a step size of 50 meV. A nonlinear least squares curve-fitting program (XPSPEAK software, Version 4.1) was used for high-resolution XPS C 1s spectral deconvolution. A Shirley-type background was chosen to be subtracted prior to quantification. After the baseline was subtracted, curve fitting was performed using an asymmetrical Gaussian–Lorentzian sum function fitting program under an optimized peak shape. For calibration purposes, the C 1s electron B.E. corresponding to graphitic carbon was set at 284.5 eV [29, 30]. This peak-fitting procedure was repeated until an acceptable fit was obtained. It was assumed that the surface composition did not vary significantly along the nanotubes, and that heterogeneity was present but at a much smaller scale than the analysis area probed by the X-ray beam.

The surface structure of MWNTs was probed by N_2 adsorption/desorption isotherms measured at −196 °C, carried out using a Micromeritics ASAP 2010 accelerated surface and porosimetry analysis system. Samples were outgassed at 350 °C overnight to remove adsorbed contaminants prior to the measurement. The measurement of N_2 adsorption data started from very low relative pressure (P/P_o was between 3.12×10^{-6} and 6.84×10^{-5}), which allowed for a meaningful assessment of the total surface area and the adsorption mechanism. The specific surface area (SSA) for the samples under study was calculated using the standard Brunauer–Emmett–Teller (BET) method on eight points of the adsorption isotherm between $0.05 < P/P_o < 0.2$. The total pore volume (V_t) was calculated by converting the amount adsorbed at a relative pressure of 0.99 to the volume of liquid adsorbate. Pore systems can be classified into three categories: macropore (>50 nm), mesopore (2–50 nm), and micropore (<2 nm) [31]. The micropore surface area (S_{mi}) and micropore volume (V_{mi}) were obtained by the t-plot method.

As in previous studies [9, 12], the PSD curves of MWNT samples in the mesopore region were determined from the desorption branches of the isotherms using the BJH methods. In this study the PSD curves were further extended to the microporous region. At the scope of micropore, the HK model was used in place of the Kelvin equation [32]. The d_s value was calculated using the modified FHH method from the adsorption data near-monolayer coverage [14, 17, 20], and the Neimark method [21] was used to calculate the d_{cc} value. The main difference between the modified FHH model and the multilayer adsorption model is that the former assumes substrate-adsorbate interactions dominate over the adsorbate-adsorbate interactions [23].

Results and discussion

HRTEM images

The HRTEM images of the MWNT samples before and after modification are shown in Fig. 1a–n. All samples had a hollow tubular structure, ranging from 10 to 80 nm in diameter and up to several micrometers in length. They consisted of well-ordered graphitic crystallites, and their inner widths were mostly one-third of the outer diameter (Fig. 1a–b). HRTEM observation revealed that the growth mechanism of as-received MWNTs was probably the base growth model, so that one end of the tube was closed and the

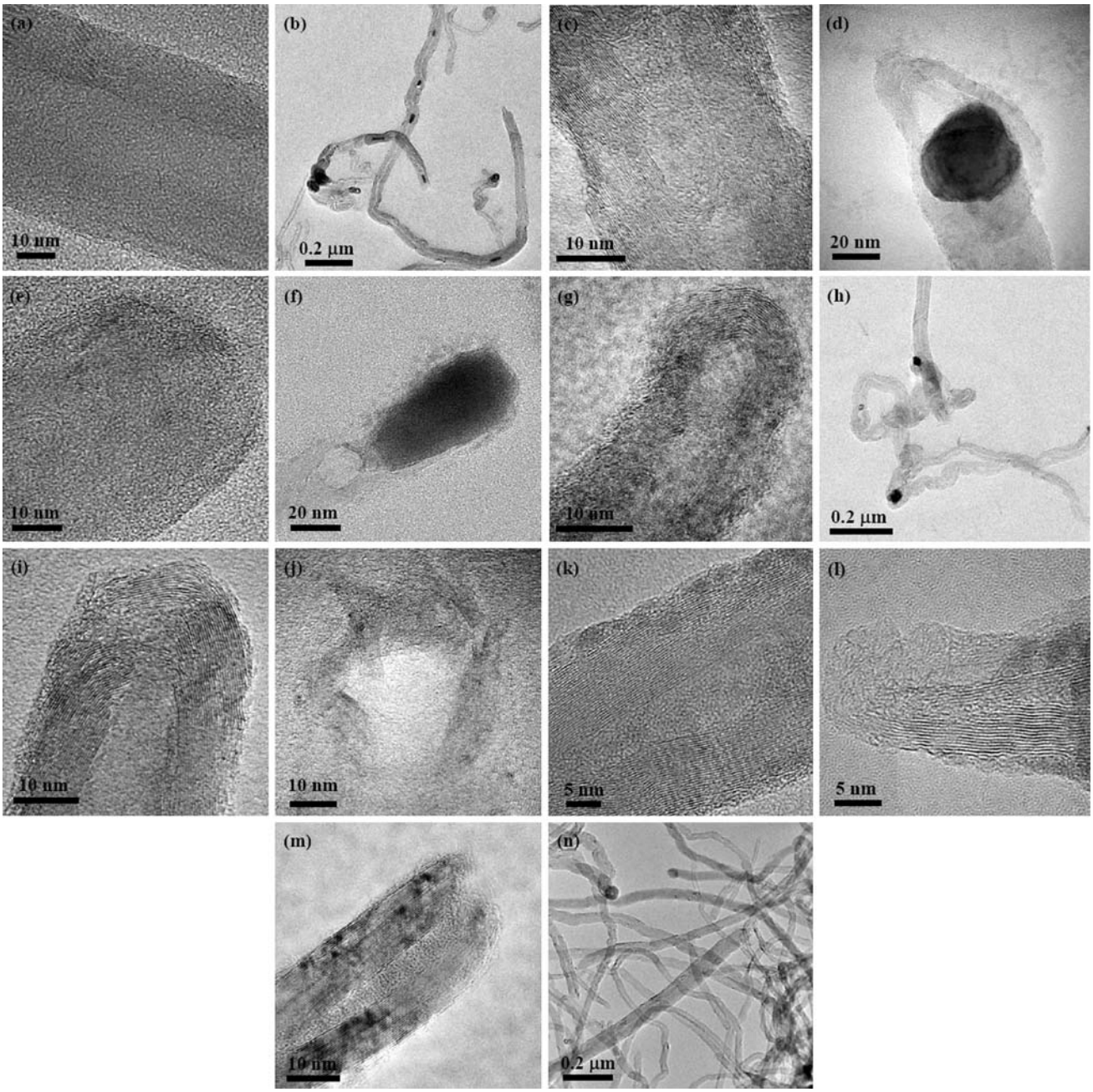

Fig. 1 HRTEM images of the multi-walled carbon nanotubes. **a**, **b** CBT; **c**, **d** CBT-Ar; **e**, **f** CBT-CO_2; **g**, **h** CBT-Vac; **i**, **j** CBT-S; **k**, **l** CBT-N; **m**, **n** CBT-SN

other was open. Some of the catalyst particles still remained in the ends of the tubes or in the hollow parts of the tubes.

The treated MWNT samples showed clear morphological changes along the tube walls or at the tips under HRTEM study. Both the heat treatment and the acid oxidation could generate a defective cylindrical graphene sheet and form the disordered carbon coating the exterior of the tubes. CBT-Ar and CBT-Vac had significant defect sites on the walls (Fig. 1c–d and g–h). In addition to the wall destruction, the tip opening of the tubes could be caused by treatment with carbon dioxide (Fig. 1e–f) or acid treatment (Fig. 1i–n). Furthermore, the acid solutions containing the sulfuric acid seemed to more effective in removing the catalyst particles in the received MWNT samples.

XRD analysis

Figure 2 compares the XRD patterns of the MWNTs subjected to different treatments. There were four characteristic peaks in all samples, which reveal that the MWNTs had a

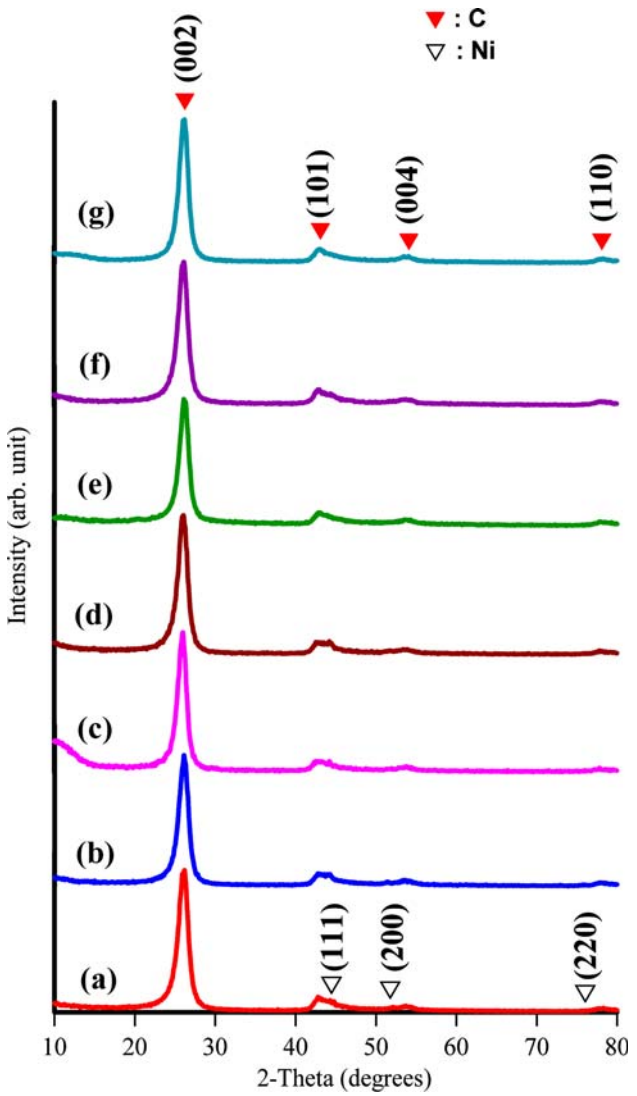

Fig. 2 XRD patterns of the as-received and treated MWNTs. (a) CBT; (b) CBT-Ar; (c) CBT-CO_2; (d) CBT-Vac; (e) CBT-S; (f) CBT-N; (g) CBT-SN

well-graphitized structure. The strongest and sharpest diffraction peak for all samples at around $2\theta = 26°$ could be indexed as the C(002) reflection of graphite, and the other three characteristic diffraction peaks of graphite at 2θ of about 43°, 54°, and 78° corresponded to C(101), C(004), and C(110), respectively, indicating that the graphite structure of the MWNTs remained intact after modification. To identify the presence of the catalyst particles, extra evidence supporting the HRTEM observations was obtained by XRD analysis. This showed one distinct diffraction peak at around $2\theta = 44°$ present in the XRD patterns of all samples except for CBT-S and CBT-SN; and two more weak peaks at 2θ of approximately 51° and 76° were also present in the XRD patterns of CBT, CBT-Ar, and CBT-Vac. The results of energy dispersive spectroscopy (not shown in this study) confirmed the presence of Ni in those samples, and so the diffraction peaks at around $2\theta = 44°$, 51°, and 76° were assigned to Ni(111), Ni(200), and Ni(220).

XPS analysis

Figure 3 shows the XPS survey scan spectra of as-received and treated MWNTs, which revealed the compositions of the most external surface of the nanotubes. The major peaks observed in the scan spectra were due to the C 1s and O 1s photoelectrons, similar to the results reported by Lee et al. [33]. The O/C atomic ratios derived from survey scan spectra were compared to see the effects of the various treatments. The O/C ratio for CBT was 0.038, close to the result reported by Liu et al. [34]. Under heat treatment to 900 °C in argon, carbon dioxide or vacuum, the O/C ratios changed to 0.036, 0.032, and 0.060, respectively. After oxidation with H_2SO_4, HNO_3 or H_2SO_4/HNO_3, the O/C ratios increased to 0.085, 0.079, or 0.045, respectively. The data thus reveal that heat treatment in argon or carbon dioxide would promote the oxygen evolution, though heat treatment in vacuum seemed to cause oxygen atom migration from inside to the surface. On the other hand, it is clear that the O/C ratios increased after acid oxidation, which indicates that the acid treatment had introduced varying amounts of surface oxides onto the MWNTs.

Deconvolution of high-resolution XPS spectra over the C 1s region for all samples was conducted. The calculated

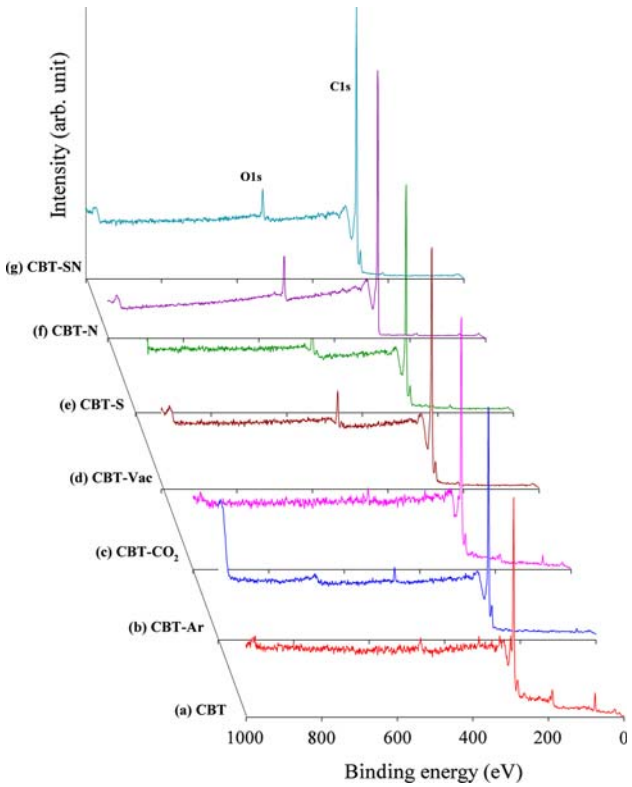

Fig. 3 XPS survey spectra of the multi-walled carbon nanotubes

percentages of graphitic and functional carbon atoms are shown in Table 1. The C 1s spectra have each been resolved into at most six individual component peaks that represent graphitic carbon (B.E. = 284.5 eV), and carbon present in phenolic, alcohol, ether or C=N groups (B.E. = 286.1 eV), carbonyl or quinone groups (B.E. = 287.3 eV), carboxyl, lactone, or ester groups (B.E. = 288.8–289.2 eV), carbonate groups (B.E. = 290.6 eV), and satellite peaks due to π–π^* transitions in aromatic rings (B.E. = 291.6 eV) [35].

Aside from graphitic carbon, phenolic groups were the most functional groups on the surface of the MWNT samples. The increase in C–OH groups resulting from the reactant attacks on graphene structure by electrophilic reactions could be considered as the generation of active sites [36]. It can be seen that the C=O groups were not observed in the samples except for CBT-Vac. As shown in Table 1, all treatments generated C–COOH groups and the MWNTs oxidized with HNO_3 possessed the most atomic percent of C–COOH groups on the tube surface. The endothermic carbon dioxide reaction did not selectively and effectively remove the corresponding initial peaks of the exothermic oxidations [37]. A possible reason for the presence of surface oxides could be caused by the initial oxidation process. The carbon dioxide was introduced in advance to the reactor for 1 h before the oxidation started in order to expel the air from the oven. When the samples contacted with carbon dioxide at room temperature, the physical adsorption of CO_2 on MWNTs could happen. Furthermore, the chemical adsorption would occur as the temperatures increased. Therefore, CBT-CO_2 would possess small amounts of surface oxides on the tubes. In addition, the data also reveal that the ability of CBT-N and CBT-SN to transform C–OH groups into C–COOH groups appeared to be better than CBT-S.

As reported in Liu et al. [34], the satellite peaks caused by π–π^* shake-up on as-received MWNTs occurred at 292.78 eV. However, after oxidization with CO_2, HNO_3, or H_2SO_4/HNO_3, the locations of these characteristic peaks were shifted to a lower B.E. (291.6 eV), and these peaks even disappeared on CBT-Ar, CBT-Vac, and CBT-S. These observations suggest a significant change in the structure of the MWNTs. The decrease or disappearance of the π–π^* transitions in aromatic rings demonstrates that the conjugated system on pristine MWNT's surface was highly stabilized and the opened ends or the defect sites generated by the treatments were almost all occupied by the surface oxides. Similar to the change in the satellite peaks, the carbonates on the surface of MWNTs decreased after treatment.

The right-most column in Table 1 shows the percent of the intensity of total surface oxides including C–OH, C–COOH, and carbonates, denoted by [O]. Except for CBT-Ar, the [O] values for all treated samples were significantly increased. But it was not expected that CBT-Vac had the highest [O] value. The possible reason for this is that the graphite crystal structure of the MWNTs was destroyed as heat-treated to 900 °C in vacuum, so that the C 1s peak had distinctly an asymmetric tailing to the higher B.E. due to the higher relative contents of the residual surface oxides. The O/C ratio of the CBT-SN obtained from its survey scan spectrum was lower than that of CBT-S or CBT-N; however, their percentages of the intensity of [O] from the fitting results of the high-resolution XPS C 1s signals were similar to each other and much higher than that of as-received MWNTs. Since the O 1s intensity could be interfered by the oxygen-containing contaminants [38], it is recommended to determine the oxygen contents by the high-resolution C 1s spectra.

N_2 adsorption isotherms

The N_2 adsorption isotherms at −196 °C on the MWNTs are shown in Fig. 4, where the amount of N_2 adsorbed is shown on a log scale in the figure so that the shape of the

Table 1 Results of the fits of the XPS C 1s region, values given in at. % of total intensity

Sample	Binding energy (eV)						% of the intensity of [O][b]
	284.5 Graphite	286.1 C–OH	287.3 C=O	288.8–289.2 C–COOH	290.6 Carbonates	291.6 π–π^*	
CBT	78.2	12.2	–	–	2.60	6.98[a]	14.8
CBT-Ar	88.9	10.3	–	0.47	0.34	–	11.1
CBT-CO_2	78.9	12.1	–	4.3	1.31	3.36	17.7
CBT-Vac	70.2	17.6	4.42	6.44	1.34	–	29.8
CBT-S	77.3	18.7	–	4.06	–	–	22.8
CBT-N	74.0	15.5	–	6.92	–	3.50	22.4
CBT-SN	75.7	14.4	–	5.35	1.50	3.03	21.3

[a] The binding energy was 292.78 eV

[b] [O] was the total surface oxides including C–OH, C–COOH, and carbonates

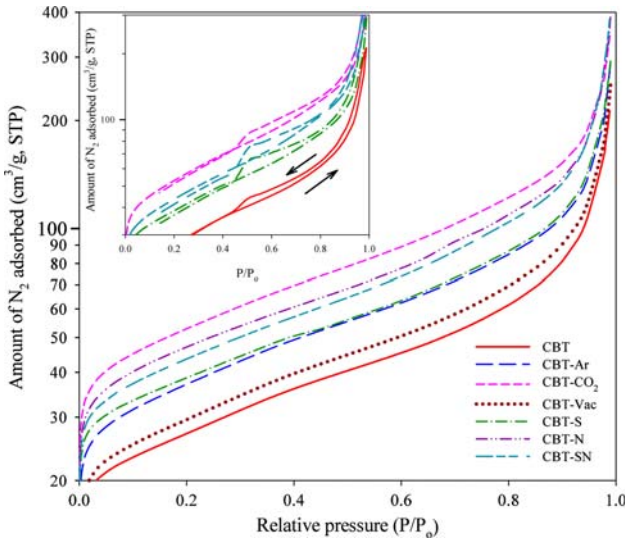

Fig. 4 N_2 adsorption isotherms for the MWNTs at −196 °C. Inset: Hysteresis loop in the adsorption–desorption isotherms for CBT, CBT-CO_2, CBT-S, and CBT-SN

adsorption curves at low pressures can be seen more readily. The adsorption isotherms were close to type II according to the BET classification, in agreement with the work of Li et al. [32], indicative of a multi-stage adsorption process. A knee on the N_2 adsorption isotherms was observed at relative pressure (P/P_o) around 0.001, describing the formation of the first coverage on the MWNTs. The large amount of adsorption on treated MWNTs at low relative pressures indicated the presence of micropores [39], which was due to the micropore filling from the enhanced adsorbate-adsorbent interactions. The isotherm over $P/P_o = 0.001$–0.45 shows a surface adsorption (or multilayer adsorption) process in which the amount of nitrogen adsorbed increased slowly.

Hysteresis loops, indicative of the formation of a capillary condensation on the substrate, were present in all MWNT samples, where some are shown in the inset of Fig. 4. Basically, the open state of the CNTs is an essential factor for the presence of the hysteresis loop. Several studies have reported the absence of hysteresis in the gas adsorption isotherm on the MWNTs; however, hysteresis clearly appeared over $P/P_o > 0.45$ on the isotherms of all samples used in this study. This indicates that the condensation and evaporation of N_2 took place at different relative pressures, which implies that some tubes had two accessible ends [40] and the MWNTs could be regarded as mesoporous materials [2]. Based on the classification of the hysteresis loops recommended by IUPAC [41], the hysteresis loops of the MWNT samples with characteristic desorption shoulders were of the type H3, different from the result of Liu et al. [9]. This reveals the porous structure of MWNTs in the mesopore range consisted of slit-shaped pores, which corresponds to the character of the layer-by-layer spacing of graphite sheets in MWNTs.

It is noteworthy that the hysteresis loops displayed a contraction at P/P_o around 0.80, and this was much more significant for the treated samples. Capillary condensation occurring over $P/P_o = 0.45$–0.80 corresponded to the pore size of 3.7–10.5 nm which indicated the inner diameter of the opened MWNTs, as illustrated by the HRTEM images. The hysteresis loop over $0.80 < P/P_o < 0.95$ showed enhanced capillary condensation in larger mesopores (10.5–38.0 nm). This is expected to be partially caused by the aggregated pores formed by the confined space among the entangled MWNTs [25]. Moreover, the areas of the hysteresis loop increased clearly on acid-treated samples, indicating that more tubes have two accessible ends after acid oxidation. On the contrary, the heat treatment showed a much weaker tendency to open the closed ends of nanotubes, which was supported by the HRTEM observations. Applying the BET model to the data yields the V_m and the SSA. Table 2 shows the surface structure data for all MWNT samples. An increase in SSA was observed after the nanotubes were modified, with an increase ranging from 10% to 97%, in the order of CBT-CO_2 > CBT-N > CBT-SN > CBT-S > CBT-Ar > CBT-Vac > CBT. This result implies the generation of the new accessible internal surfaces, probably due to tip openings or the defect sites.

PSD curves

Some authors used the BET surface area to characterize the CNTs [42, 43], while several studies [1, 44] have suggested the key feature of the CNTs should be the PSD curve. The uptake of N_2 at very low pressures is due to micropore filling, which is distinct from the adsorption mechanisms in mesopores (i.e., multilayer adsorption and capillary condensation). In this study, the PSD curves obtained from N_2 adsorption/desorption isotherms were calculated by the BJH method in the mesoporous region and by the HK method in the microporous region, as shown in Fig. 5. All samples had remarkably differential pore volumes in the ranges of micropore and mesopore. According to a recent discussion about closed MWNTs [45], the adsorption space of less than 4 nm should be contributed by the defect sites on the wall and at the end tips. As a result, the pores responsible for the N_2 adsorption should be the inner cavities of the tubes (<4 nm) and the intertubular spaces of the aggregated MWNTs (≥4 nm) since the interplanar spacing between the coaxial tubes of the MWNTs was smaller than the N_2 molecule [46].

The maximum of the PSD curve of as-received MWNTs was located about 0.9 nm, much smaller than that obtained by Li et al. [32]. In view of the surface integrity of the

Table 2 Surface structure of the as-received MWNTs and treated MWNTs determined by N_2 adsorptions

	SSA (m^2/g)	S_{mi} (m^2/g)	S_{ext} (m^2/g)	V_m (cm^3/g, STP)	V_t^a (cm^3/g)	V_{mi}^b (cm^3/g)	V_{me}^c (cm^3/g)	V_{ma}^d (cm^3/g)	Mean pore size[e] (nm)
CBT	96.24	6.93	89.31	22.12	0.3286	0.0029	0.2023	0.1234	13.66
CBT-Ar	133.01	6.67	126.34	30.55	0.4434	0.0022	0.2366	0.2046	13.33
CBT-CO_2	189.87	11.72	178.15	43.62	0.5411	0.0040	0.3323	0.2048	11.40
CBT-Vac	105.92	5.95	99.98	24.33	0.3901	0.0021	0.1971	0.1908	14.73
CBT-S	137.17	18.05	119.13	31.51	0.4524	0.0078	0.2705	0.1741	13.19
CBT-N	168.95	13.69	155.26	38.81	0.6089	0.0050	0.3403	0.2636	14.42
CBT-SN	156.22	12.24	143.98	35.89	0.6003	0.0045	0.3151	0.2807	15.37

[a] V_t represented the single point total pore volume at $P/P_o \approx 0.99$

[b] V_{mi} was determined by t-plot method

[c] V_{me} was calculated by BJH method

[d] V_{ma} was found by subtracting V_{me} and V_{mi} from V_t

[e] Mean pore size was obtained by $4V_t$/SSA

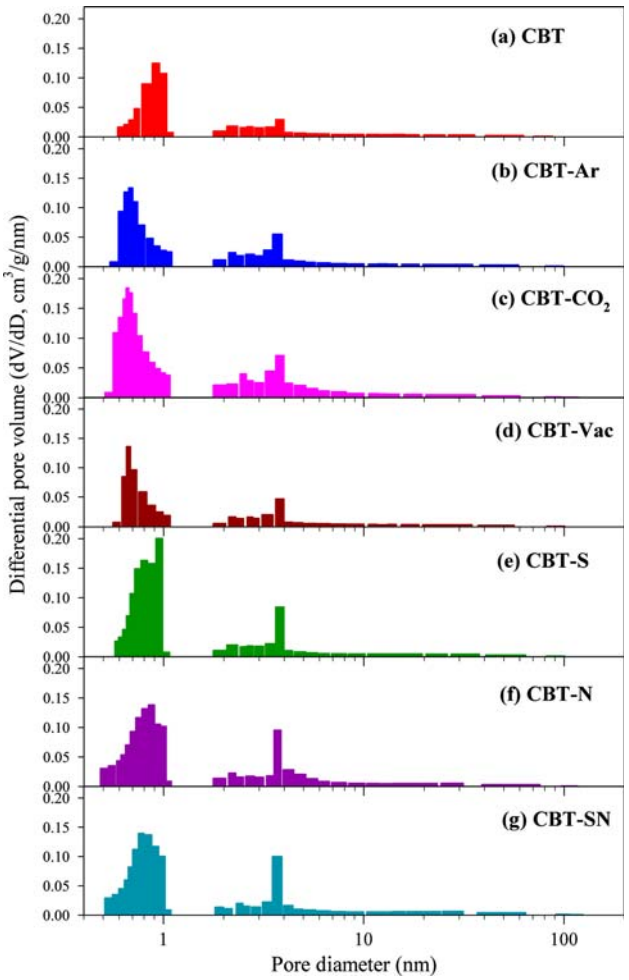

Fig. 5 Pore size distributions of the MWNT samples from N_2 adsorption/desorption isotherms

original MWNT samples, it was expected that these small cracks on the samples appeared in the open ends of the nanotubes. In addition, there was another peak at around 3.8 nm in the PSD curve of CBT, which could be assigned to the major inside diameter of the nanotubes and has been verified by the HRTEM images. The changes in the pore structures can be easily seen from the PSD curves of the treated MWNT samples. After heat treatment, the maximum of the PSD curves was shifted slightly downwards to 0.7 nm and the shapes of the micropore distributions varied significantly. It is believed that these micropores originated from the new defect sites on the surface and the enlargement of small defects by heat treatment. Nevertheless, the peak pore size in mesopore region remained distinct at 3.8 nm. On the other hand, the PSD curves of the acid-treated MWNTs showed a maximum at the pore size of 0.8–0.95 nm. The intensities of their micropore distributions were much higher than that of CBT but these four micropore distributions had similar shapes, which indicated the generation of new micropores. Meanwhile, there was also a distinct peak at a pore size of 3.8 nm in the PSD curves of the acid-treated samples, in which the peak intensities were over 2-fold of the CBT. It is believed that the increase in the peak intensity at a pore size of 3.8 nm should be indicative of the opening of the closed ends of nanotubes by acid oxidation.

The calculated pore volumes are also shown in Table 2. Mesoporosity was dominant in all MWNT samples with a mesopore volume (V_{me}) over 50–62%, similar to the results in Liu's study [9]. In comparison with CBT, the macropore volumes (V_{ma}) in the heat-treated samples had an increase of about 60%; whereas in mesopore or micropore ranges, only CBT-CO_2 presented a noticeable increase, 64% for V_{me} and 40% for V_{mi}. In CBT-S, there was only a 30–40% increase in V_{ma} and V_{me}, but its V_{mi} increased by 163%. For CBT-N and CBT-SN, the V_{me} (or V_{mi}) increased about by 70 and 55%, respectively, even though the increased porosity was mainly contributed by macropores, over 100% increment.

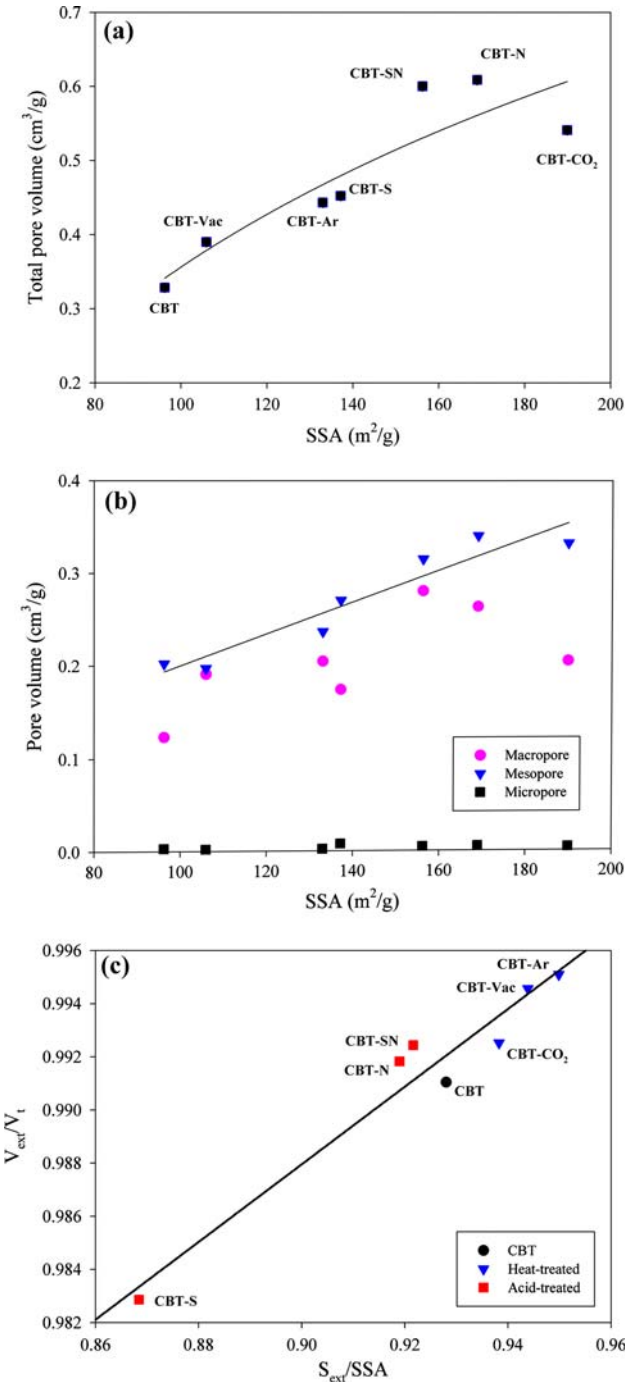

Fig. 6 Changes in pore volumes of the MWNTs with their BET specific surface areas

Figure 6a shows that the total pore volumes of all samples were positively proportional to their BET SSAs. The data distribution revealed that the heat treatment tended to increase the surface area, but the acid treatment not only generated much more surface area but also developed inner pore structures. In Fig. 6b, the pore structure has been classified into three groups: micropore, mesopore, and macropore. It is clear that the V_{me} could be represented by a linear function of SSA. But there was no causal relationship between SSA with V_{ma} and V_{mi}. This conclusion exactly corresponds to the nature of mesoporosity. If the sum of S_{ma} and S_{me} was defined by the external surface area (S_{ext}) and the sum of V_{ma} and V_{me} was defined by the external pore volume (V_{ext}), Fig. 6c illustrates the ratio of V_{ext} to V_t varied almost linearly with the ratio of S_{ext} to SSA. It is especially true that the heat-treated samples and the acid-treated samples were located on the different ends along this line with respect to the untreated MWNT. That is, the heat-treated samples had higher S_{ext}/SSA and V_{ext}/V_t values, which indicates that the heat treatment was beneficial to the formation of mesopores and macropores in the order of CBT-Ar > CBT-Vac > CBT-CO_2. In contrast, the acid-treated samples had lower S_{ext}/SSA and V_{ext}/V_t values and revealed that the acid oxidation had a higher potential to generate micropores, in the order of CBT-S ≫ CBT-N > CBT-SN.

Surface fractal analysis

Fractal dimension analysis was performed on all N_2 adsorption isotherms. Figure 7a shows the plot drawn with the standard coordinates of $\ln(V/V_m)$ versus $\ln[\ln(P_o/P)]$ from the near-monolayer coverage section of the measured N_2 adsorption isotherm ($1 < V/V_m < 2$) according to the modified FHH theory. The slope of the modified FHH plot was used for calculating the d_s value. In addition, the d_{cc} value was calculated from the capillary condensation region of the N_2 adsorption isotherm according to the Neimark's equation. The relationships between S and r for all samples are plotted in Fig. 7b in double-logarithmic scales. The lower limit for r where linearity was present in all samples was approximately 0.35 nm, corresponding to the limit of applicability of the Kelvin equation. The upper limit for r was about 16.7–17.7 nm, which agrees fairly well with the results of Hou [16], except for the original CNTs. The d_{cc} values could be calculated from the slopes of those fitting lines.

Figure 8 illustrates the changes of the d_s and the d_{cc} with SSA. The d_s values (the solid symbols) ranged from 2.51 to 2.56, close to the published data of MWNTs [24], indicating self-similarity of the nanotube surface [23]. The d_s values of the heat-treated MWNTs were lower than that of the original sample, indicating a smoother surface can be achieved by heat treatment. Moreover, the surface roughness of the heat-treated samples seemed to increase with their SSAs. On the other hand, the d_s values of the acid-treated samples were higher than those of CBT and the heat-treated, which was in good agreement with the study of Kanyó et al. [24]. This is indicative of the destruction of surface integrity by acid oxidation because of the opened end tips or the defects on the walls or the attachment of the

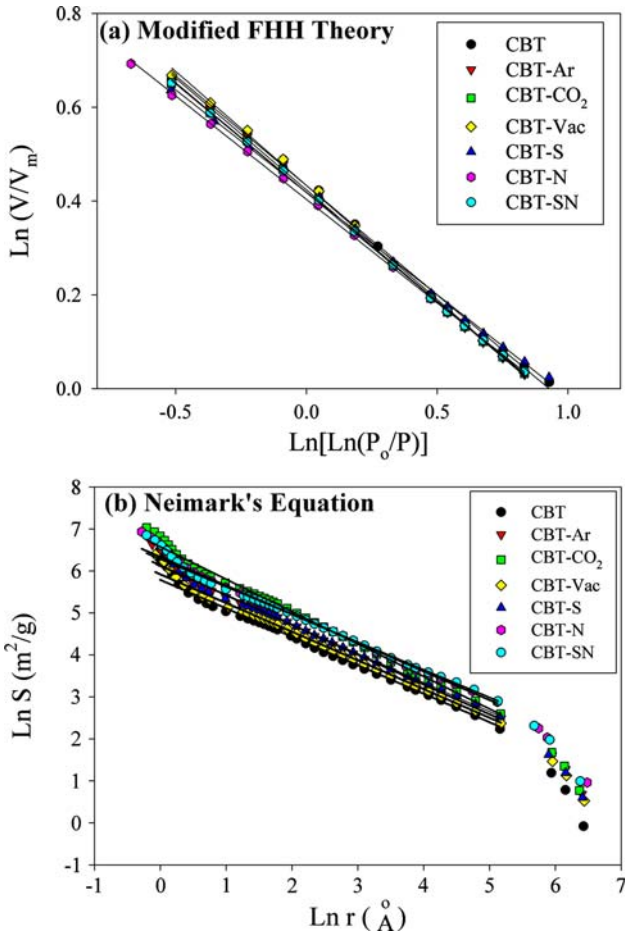

Fig. 7 Plots drawn with the standard coordinates of **a** $\ln(V/V_m)$ versus $\ln[\ln(P_o/P)]$ and **b** $\ln S$ versus $\ln r$, from the measured N_2 adsorption isotherms on the MWNT samples. The straight lines correspond to the linear regression in the scale range of possible fractality

surface oxides, resulting in the increased surface roughness. Figure 9a shows a clearly linear increase in the S_{mi} as the d_s values increased, which suggests that the generation of micropores would contribute to the surface roughness.

Based on the broad PSD (Fig. 5) and partially closed ends as well as tube entanglement (Fig. 1), the MWNTs were generally regarded as small d_{cc} materials [23]. The d_{cc} values (between 2.65 and 2.75) were higher than the corresponding d_s values, which agreed with the study of Kukovecz et al. [23]. The plot of the d_{cc} versus SSA for the MWNT samples, in Fig. 8, can also be divided into two groups. The d_{cc} values of all samples except those with acid treatment were positively linear proportional to the SSA. Contrary to the results on the d_s values, the d_{cc} values of the acid-treated samples were smaller than those of the heat-treated on the same resulting SSA level. As suggested by Armatas et al. [47], higher d_{cc} values represent more ordered pore systems. Accordingly, the d_{cc} values indicated that on the same resulting SSA level the MWNTs by heat treatment

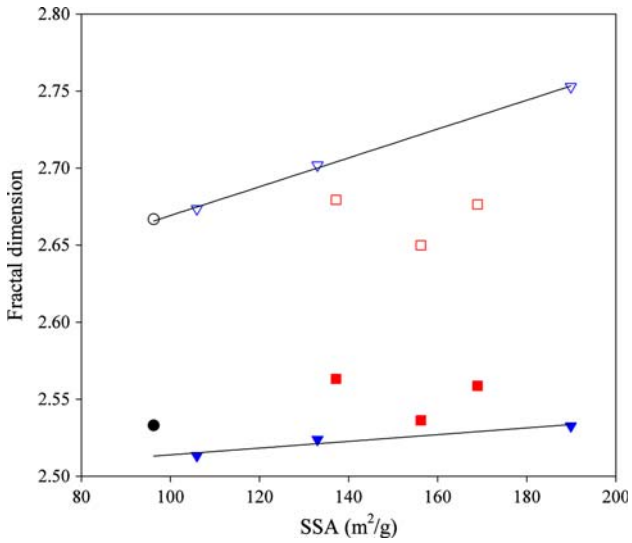

Fig. 8 Relationships of BET specific surface area (SSA) with the surface fractal dimension (d_s, the solid symbols) and the dimension of the capillary condensation (d_{cc}, the hollow symbols), where circle (filled circle/open circle): CBT; triangle (filled reversed triangle/open reversed triangle): heat-treated samples; square (filled square/open square): acid-treated samples

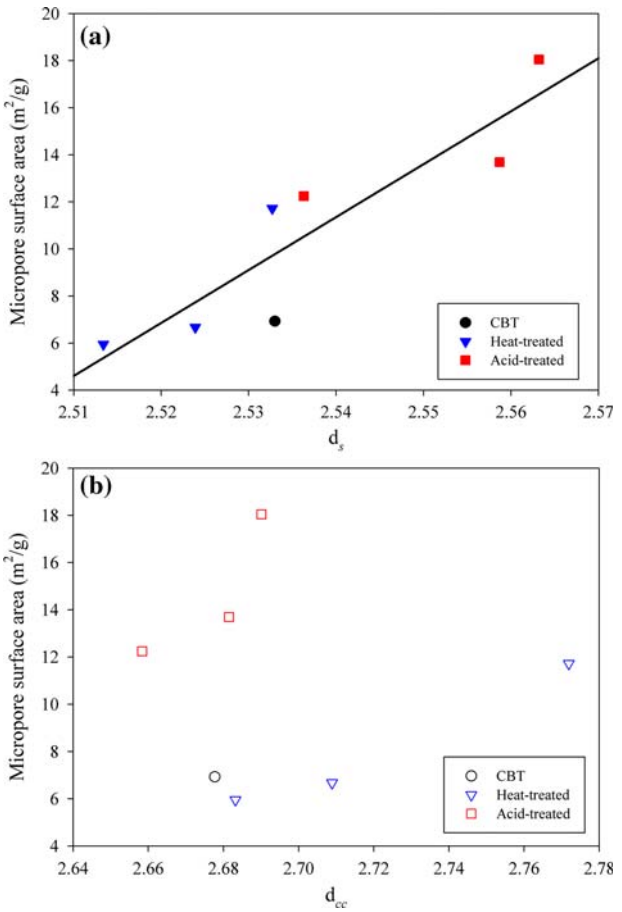

Fig. 9 Variation of micropore surface area with the fractal dimensions. **a** d_s; **b** d_{cc}

could acquire a more uniform pore structure, while the acid oxidation would make the MWNTs have a more irregular pore system. As mentioned before, the heat-induced disorder has made CBT-Vac have the lowest d_{cc} value among the heat-treated samples. Figure 9b shows the relationship between the S_{mi} and the d_{cc}, where two branches were observed depending on whether heat treatment or acid oxidation had been used. No matter what treatment was used, a larger S_{mi} brought a higher d_{cc} value, similar to the d_s values.

It is worth noting that the fractal dimension data in Fig. 8 had two limit boundaries with respect to the resulting SSA, which were composed of the d_s and the d_{cc} values of the heat-treated samples. Accordingly, the side wall defects and the end cap opening would enhance the surface roughness, and the attachment of the surface functional groups was expected to block the entrance to the micropores and generate an irregular pore system. Furthermore, a new, relatively slippery and more ordered surface could be formed after heat treatment.

No matter on the d_s or d_{cc} values, the changes in the surface properties after heat treatment exhibited similar effects. This can also be seen on the acid-treated samples. As mentioned before, the increase in surface area and pore volume resulted in the increase in the fractal dimensions. As the average pore size or the V_t/V_m ratio (i.e., the number of adsorbed layer) became larger, the fractal dimensions would become smaller. This means the increase in the number of adsorbed layers indicated a smoother surface and a broader PSD curve. On the other hand, as the V_{ma} increased due to the heat treatment, the d_s (or d_{cc}) value increased; while in a similar situation due to the acid treatment, the d_s (or d_{cc}) value dropped. Furthermore, when the O/C ratio or the percentage of C–OH decreased due to the heat treatment, the d_s (or d_{cc}) value would increase. But in a similar situation due to the acid treatment, the d_s (or d_{cc}) value decreased. It is believed that the pore-blocking effect of the surface functional groups was present only when the samples were acid-treated. It also indicates that the influence of the modification approaches was much more significant than the difference between the fractal dimensions (d_s and d_{cc}).

Conclusions

Oxidation by the solutions containing H_2SO_4 associated with the post-heat treatment was a promising method to removal of the catalyst particles, in addition to making the samples dried completely. The acid solutions involving HNO_3 had a higher potential to attach C–COOH groups onto the surface of the MWNTs without a significant loss of the graphitic crystallinity. After heat treatment to 900 °C in CO_2, the MWNTs could maintain good crystallinity and have C–COOH groups on the surface due to the low temperature contact. On the contrary, the crystallinity of the MWNTs would be significantly damaged when heat-treated to 900 °C in vacuum. The N_2 adsorption on the MWNTs was a multi-stage adsorption process. The MWNTs contained micropores, mesopores, and macropores so that the volume filling of micropores occurred first at low pressures and was followed by the formation of a multilayer film on the mesopore walls, and next the remaining empty space inside mesopores was filled by a capillary condensation process. The hysteresis loops with a contraction characterized the adsorption mechanisms of the MWNTs in the capillary condensation region: the internal pores first and followed by the aggregated pores forming by the confined space among the entangled MWNTs. The acid oxidation of the MWNTs generated much more micropores and introduced C–COOH groups onto the surface in addition to end cap opening, while the heat treatment of the MWNTs mainly contributed to the external pores. Fractal analysis was a useful method to investigate the surface properties of the MWNTs after treatment. The surface roughness and the pore system were well characterized by the d_s and d_{cc} values. This study confirmed that N_2 adsorption is a convenient and powerful method to characterize the structural and surface properties of the MWNTs and it is therefore very useful in the prediction of gas adsorption properties of the MWNTs.

Acknowledgements The authors gratefully thank the National Science Council (NSC) of Taiwan for financial support, through Project No.: NSC 93-2211-E-155-003. The authors also thank the Precision Instrument Center of the NSC for the support of experimental instruments used in this study.

References

1. Li Z, Pan Z, Dai S (2004) J Colloid Interface Sci 277:35
2. Inoue S, Ichikuni N, Susuki T, Uematsu T, Kaneko K (1998) J Phys Chem B102(24):4689
3. Hilding J, Grulke EA, Sinnott SB, Qian D, Andrews R, Jagtoyen M (2001) Langmuir 17:7540
4. Huang WZ, Zhang XB, Tu JP, Kong FZ, Ma JX, Liu F, Lu HM, Chen CP (2002) Mater Chem Phys 78:144
5. Babaa MR, Stepanek I, Masenelli-Varlot K, Dupont-Pavlovsky N, McRae E, Bernier P (2003) Surf Sci 531:86
6. Sahaym U, Norton MG (2008) J Mater Sci 43:5395. doi:10.1007/s10853-008-2749-0
7. Chang Q, Zhao K, Chen X, Li M, Liu J (2008) J Mater Sci 43:5861. doi:10.1007/s10853-008-2827-3
8. Byl O, Kondratyuk P, Forth ST, FitzGerald SA, Chen L, Johnson JK, Yates JT Jr (2003) J Am Chem Soc 125:5889
9. Liu ZT, Wang CX, Liu ZW, Lu J (2008) Appl Catal A344:114
10. Hilding JM, Grulke EA (2004) J Phys Chem B108:13688
11. Hu YH, Ruckenstein E (2004) Ind Eng Chem Res 43:708
12. Li L, Wu G, Xu BQ (2006) Carbon 44:2973
13. Lee GW, Lee JI, Lee SS, Park M, Kim J (2005) J Mater Sci 40:1259. doi:10.1007/s10853-005-6947-8

14. Wu MK (1996) Aerosol Sci Technol 25(4):392
15. Lee WH, Reucroft PJ (1999) Carbon 37:7
16. Hou QF, Lu XC, Lu ZJ, Liu XD (2005) Colloid Surf A264:219
17. Tang P, Chew NYK, Chan HK, Raper JA (2003) Langmuir 19:2632
18. Sen D, Mazumder S, Chitra R, Chandrasekaran KS (2001) J Mater Sci 36:909. doi:10.1023/A:1004899017679
19. Sen D, Mazumder S, Tarafdar S (2002) J Mater Sci 37:941. doi:10.1023/A:1014391629262
20. Pfeifer P, Wu YJ, Cole M, Krim J (1989) Phys Rev Lett 62:1997
21. Neimark AV (1992) Physica A191:258
22. Gregg SJ, Sing KSW (1982) Adsorption, surface area and porosity, 2nd edn. Academic Press, London
23. Kukovecz A, Kanyo T, Konya Z, Kiricsi I (2005) Carbon 43:994
24. Kanyo T, Ko′nya Z, Kukovecz A, Berger F, De′ka′ny I, Kiricsi I (2004) Langmuir 20:1656
25. Yang QH, Hou PX, Bai S, Wang MZ, Cheng HM (2001) Chem Phys Lett 345:18
26. Horvath G, Kawazoe K (1983) J Chem Eng Jpn 16:470
27. Lago RM, Tsang SC, Lu KL, Chen YK, Green MLH (1995) J Chem Soc Chem Commun 13:1355
28. Moulder JF, Stickle WF, Sobol PE, Bomben KD (1992) In: Chastain J (ed) Handbook of x-ray photoelectron spectroscopy. Perkin-Elmer Corporation, Eden Prairie, MN
29. Biniak S, Szymanski G, Siedlewski J, Swiatkowski A (1997) Carbon 35(12):1799
30. Okpalugo TIT, Papakonstantinou P, Murphy H, McLaughlin J, Brown NMD (2005) Carbon 43:153
31. IUPAC Manual of Symbols and Terminology, Appendix 2, Part 1, Colloid and Surface Chemistry (1972) Pure Appl Chem 31:578
32. Li F, Wang Y, Wang D, Wei F (2004) Carbon 42:2375
33. Lee WH, Kim SJ, Lee WJ, Lee JG, Haddon RC, Reucroft PJ (2001) Appl Surf Sci 181:121
34. Liu Y, Shen Z, Yokogawa K (2006) Mater Res Bull 41:1503
35. Moreno-Castilla C, Lopez-Ramon MV, Carrasco-Marin F (2000) Carbon 38:1995
36. Zhang J, Zou H, Qing Q, Yang Y, Li Q, Liu Z, Gou X, Du Z (2003) J Phys Chem B107:3712
37. Smith MR Jr, Hedges SW, LaCount R, Kern D, Shah N, Huffman GP, Bockrath B (2003) Carbon 41:1221
38. Tsai MY, Sun YT, Lin JC (2007) J Colloid Interface Sci 308:474
39. Lee SM, Lee SC, Jung JH, Kim HJ (2005) Chem Phys Lett 416:251
40. Mackie EB, Wolfson RA, Arnold LM, Lafdi K, Migone AD (1997) Langmuir 13:7197
41. Zhdanov VP (1993) Adv Catal 39:1
42. Bacsa RR, Laurent Ch, Peigney A, Bacsa WS, Vaugien Th, Rousset A (2000) Chem Phys Lett 323:566
43. Cinke M, Li J, Chen B, Cassell A, Delzeit L, Han J, Meyyappan M (2002) Chem Phys Lett 365:69
44. Eswaramoorthy M, Sen R, Rao CNR (1999) Chem Phys Lett 304:207
45. Furmaniak S, Terzyk AP, Gauden PA, Lota K, Frąckowiak E, Béguin F, Kowalczyk P (2008) J Colloid Interface Sci 317:442
46. Yang K, Xing B (2007) Environ Pollut 145:529
47. Armatas GS, Salmas CE, Louloudi M, Androutsopoulos GP, Pomonis PJ (2003) Langmuir 19:3128